

A study of the *Fermi* bubbles near the Galactic plane

L. Herold ^{*1} and D. Malyshev ^{**1}

Erlangen Centre for Astroparticle Physics, Erwin-Rommel-Str. 1, Erlangen, Germany

Received September 15, 1996; accepted March 16, 1997

ABSTRACT

Context. *Fermi* bubbles are one of the most unexpected discoveries by the *Fermi* LAT. At the moment the origin of the bubbles and the nature of the gamma-ray emission are still unresolved questions. The behavior of the bubbles near the Galactic plane may have an important clue to solve the question of the origin of the bubbles.

Aims. We analyze 8 years of the *Fermi* LAT pass 8 data to study the morphology and spectrum of the *Fermi* bubbles near the Galactic plane.

Methods. We use several methods to separate the emission from the bubbles from the Galactic foreground diffuse emission and the contribution from point sources.

Results. We confirm that the *Fermi* bubbles have a higher intensity of gamma-ray emission near the GP relative to high latitudes, the emission is shifted to the west (negative longitudes) from the GC. The spectrum is consistent with a single power law up to 1 TeV

Key words. Gamma rays: general – Galaxy: center – Galaxy: halo – ISM: jets and outflows

Contents

1	Introduction	1
2	Data selection	1
3	Modeling of the <i>Fermi</i> bubbles at low latitudes	2
3.1	Left-right difference in the data	2
3.2	Low energy data as a background model . .	2
3.3	Rectangles model of the bubbles	3
3.4	GALPROP model of the foreground and PS refitting	3
4	Discussion	3
4.1	Profile plots	3
4.2	Comparison of the spectra at different latitudes	4
4.3	IC model	4
4.4	Pion model	4
5	Conclusions	4
A	Appendix	8

1. Introduction

Discussion of the *Fermi* bubbles properties at high latitudes.

Discussion of the models of the bubbles. Motivate the study at low latitudes.

Discuss the previous results – hints for higher intensity and harder spectrum near the GP, also the asymmetry with respect to the GC.

Main goal of this paper - analysis of the *Fermi* bubbles within 10° from the GP. Especially at high energies.

2. Data selection

The main goal of the analysis is a study of a relatively small region $\lesssim 10^\circ$ from the GC for energies $\gtrsim 1$ GeV, we choose the *Fermi* LAT Pass 8 Source class events as our main data sample. We use 9 years of *Fermi*-LAT data between August 4, 2008 and August 3, 2017 (*Fermi* Mission Elapsed Time 239557418 s–523411376 s) with energies between 316 MeV $= 10^{2.5}$ MeV and 1 TeV separated in 21 logarithmic energy bins (6 bins per decade). We use the standard quality cuts To avoid contamination from cosmic ray interactions in the Earth atmosphere, we select events with an angle $\theta < 100^\circ$ with respect to the local zenith. This zenith angle cut is sufficient for energies above 316 MeV. We calculate the exposure and PSF using the standard *Fermi* LAT Science Tools package version 10-01-01 available from the *Fermi*

* e-mail: laura.herold@fau.de

** e-mail: dmitry.malyshev@fau.de

Science Support Center¹ using the P8R2_SOURCE_V6 instrument response functions. For spatial binning we use HEALPix² (Górski et al. 2005) scheme with a pixelization of order 7 (≈ 0.46 pixel size).

3. Modeling of the *Fermi* bubbles at low latitudes

One of the main problems in the analysis of the FB near the GC is the presence of the foreground emission components, such as the interactions of cosmic rays with the interstellar gas and radiation fields. In order to test the possible effects of the foreground emission modeling, we use several methods to estimate the contribution of the foreground emission to the data.

In particular, there is a tentative displacement of the FB to the right of the GC, e.g., negative Galactic latitudes (Acero et al. 2016; Ackermann et al. 2017), with a spectrum that is harder than the spectrum of the FB at high latitudes (Ackermann et al. 2017). If we assume that the Galactic emission components are approximately symmetric with respect to the GC, then we can simply mask PS and calculate the difference in gamma-ray flux to the left and to the right from the GC. The difference should be approximately equal to the asymmetric part of the FB emission under the assumption that the other Galactic components and unresolved PS are symmetric with respect to the GC (Section 3.1).

In order to further test the hypothesis of the asymmetric and hard emission from the FB at low latitudes, we use the data at energies $\lesssim 1$ GeV to create a template of the Galactic emission, provided that the expected contribution of the FB at these energies is small relative to the rest of the Galactic components. Then we fit the template derived from the low energy data together with an isotropic template at higher energies outside of the FB area. The FB intensity is determined by extrapolating the model inside the FB area using the full template and by subtracting the model from the data (Section 3.2). As an alternative approach, instead of fitting outside of the FB area, we add independent flat rectangular templates with the size approximately following the FB size to the model and fit over the whole sky. The flux attributed to these rectangular templates is used as an estimate of the average flux in the FB in the corresponding areas (Section 3.3).

We also calculate the flux attributed to the bubbles using one of the diffuse emission models from (Ackermann et al. 2017) (Section 3.4).

3.1. Left-right difference in the data

As a first simple check of the asymmetry at low latitudes, we compare the unprocessed *Fermi*-LAT data east and west

of the Galactic center. After masking PS, we average the data over a region west, i.e. longitudes $\ell \in (-10^\circ, 0^\circ)$, and east, i.e. $\ell \in (0^\circ, 10^\circ)$, of the Galactic center for different latitudes. The regions have a width of 10° in latitude for high latitudes, $b > |10^\circ|$, and 4° for low latitudes, $b < |10^\circ|$. The difference of the averaged diffuse emission west – east is shown in Fig. 1 as a function of energy. At high latitudes, $b > |10^\circ|$, the emission is very symmetric. The emission for latitudes $b \in (-6^\circ, -2^\circ)$ and $b \in (-2^\circ, 2^\circ)$ shows excessive emission west of the Galactic center, which does not decay for high energies.

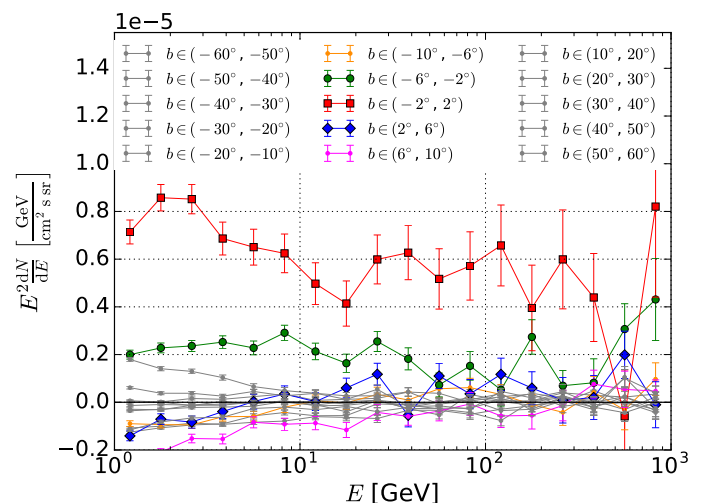


Fig. 1: Difference west – east in the unprocessed *Fermi*-LAT data with symmetric PS mask. The region west reaches from -10° to 0° longitude, the region east from 0° to 10° longitude.

3.2. Low energy data as a background model

Gamma rays produced in interactions of CR with gas and IC scattering dominate the gamma-ray emission around the GC in the energy range $E \lesssim 1$ GeV. Consequently, low-energy *Fermi*-LAT data is a good tracer for diffuse gamma-ray emission in the Galactic plane and can be used to create a spatial template for the Galactic foreground. Since the angular resolution is worse for smaller energies, we smooth the data in each high-energy bin with a Gaussian kernel of 1° to compensate for the difference in angular resolution.

We cut the sky horizontally in latitude stripes with the width of 4° and define our model in each stripe and energy bin separately. In the latitude stripe ℓ and energy bin E our model consists of a term proportional to the low-energy photon counts $k_{\ell\alpha} \cdot \tilde{N}_\ell^{\text{low}}(E, x)$, summed over all energies in 0.3 - 1.0 GeV, and an additional term $\tilde{c}_\ell(E, x)$:

$$N_\ell^{\text{model}}(E, x) = k_\ell(E) \cdot \tilde{N}_\ell^{\text{low}}(E, x) + \tilde{c}_\ell(E, x). \quad (1)$$

¹ <http://fermi.gsfc.nasa.gov/ssc/data/analysis/>

² <http://sourceforge.net/projects/healpix/>

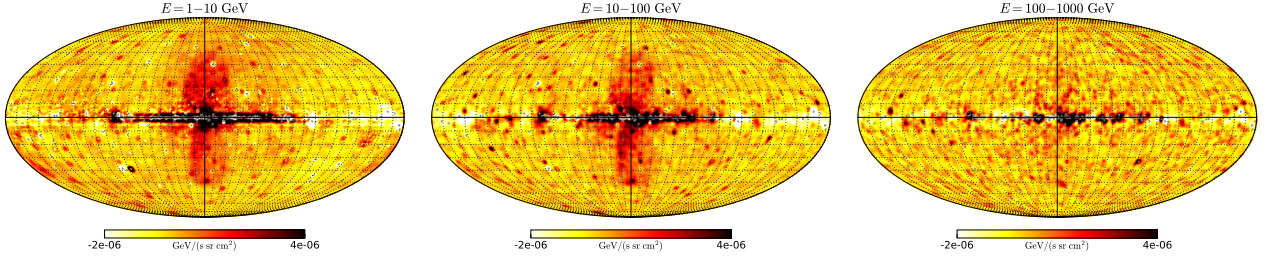


Fig. 2: Residuals of the low-energy model for three different energy ranges. The *Fermi* bubbles are clearly visible in the first two energy ranges. Point sources are masked.

The term $\tilde{c}_\ell(E, x)$ consists of a factor $c_\ell(E)$, which is constant in each latitude ℓ and energy E , that is weighted by the exposure $\tau(E, x)$:

$$\tilde{c}_\ell(E, x) = c_\ell(E) \cdot \tau(E, x). \quad (2)$$

It takes into account the isotropic extragalactic background and partially compensates for the latitude dependent IC emission. To include the dependence of exposure on energy and position in the sky, the low-energy data is weighted by the quotient of exposure $\tau(E, x)$ in the low- and high-energy range in each pixel x :

$$\tilde{N}_\ell^{\text{model}}(E, x) = \frac{1}{n_{\text{low}}} \left(\sum_{\epsilon \in (0.3-1.0 \text{ GeV})} \frac{N^{\text{low}}(\epsilon, x)}{\tau(\epsilon, x)} \right) \cdot \tau(E, x), \quad (3)$$

where n_{low} is the number of low-energy bins.

We determine the parameters $c_\ell(E)$ and $k_\ell(E)$ by fitting the model to the *Fermi*-LAT data in energy bins $E > 1.0 \text{ GeV}$ using Poisson likelihood (with Python *iminuit* minimizer). Since we smooth the data before the fit, the Poisson log-likelihood is an approximation in this case. To avoid an overcompensation of the *Fermi* bubbles the region $-20^\circ < \ell < 20^\circ$ is excluded from the fit. We mask the 200 brightest 3FGL PS with a circle of radius $\frac{\delta}{\sqrt{2}} + 1^\circ$ where $\delta = 0.46^\circ$ is the characteristic size of the pixels. We also symmetrize the PS relative to the GC in order to avoid possible bias by masking more pixels on one side of the GC.

After we fit the model in each latitude stripe, we interpolate it inside the bubbles ROI and find the residual by subtracting it from the data. Figure 2 shows the residual maps for three different energy ranges. The FB are clearly visible in the first two energy ranges, $E = 1 - 10 \text{ GeV}$ and $E = 10 - 100 \text{ GeV}$, for $E = 100 \text{ GeV} - 1 \text{ TeV}$ the statistics is low, but one can still see an excess near the GP.

3.3. Rectangles model of the bubbles

Our first simple ansatz for a model of the FB consists of rectangular templates that approximately cover the area of the FB. As a model for the foreground we again use

the low-energy model from Section 3.2. As before, the fit is performed independently in each 4° latitude stripe. To explore the east-west asymmetry of the FB, two rectangular templates, one east ($-20^\circ - 0^\circ$) and one west ($0^\circ - 20^\circ$), are added to the low-energy model in each latitude stripe ℓ and energy bin E :

$$N_\ell^{\text{model}}(E, x) = k_\ell(E) \cdot \tilde{N}_\ell^{\text{low}}(E, x) + \tilde{c}_\ell(E, x) + R_\ell^{\text{east}}(E) + R_\ell^{\text{west}}(E). \quad (4)$$

We determine the normalization of the rectangles $R_\ell^{\text{east}}(E)$ and $R_\ell^{\text{west}}(E)$ and the parameters $k_\ell(E)$ and $c_\ell(E)$ by fitting the model to the *Fermi*-LAT data in energy bins $E > 1.0 \text{ GeV}$. The resulting residual, shown in Fig. 3 for $E = 10 - 100 \text{ GeV}$, is very similar to the low-energy model.

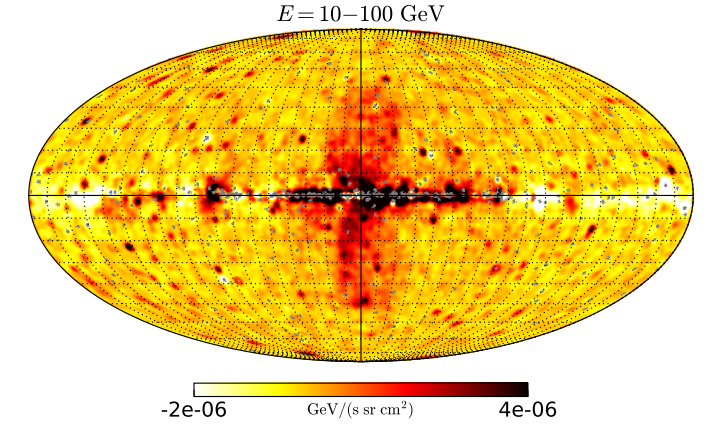


Fig. 3: Rectangles-model residual.

3.4. GALPROP model of the foreground and PS refitting

4. Discussion

4.1. Profile plots

Figure 5 shows the latitude profiles of the different models in differential flux. The flux increases towards the Galactic plane. Left-right asymmetry close to the Galactic center.

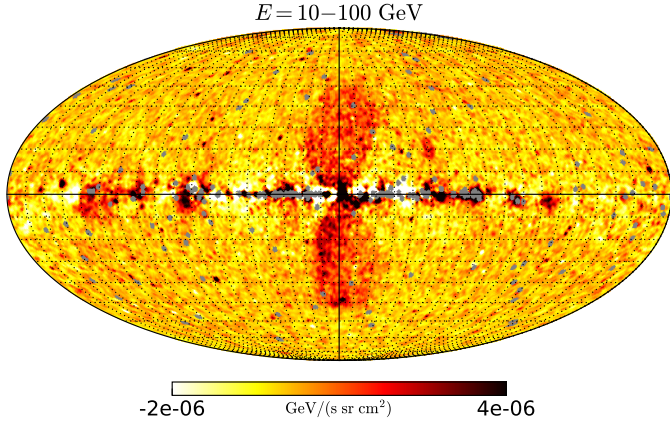


Fig. 4: GALPROP-model residuals in three different energy ranges.

4.2. Comparison of the spectra at different latitudes

Figure 6 shows a comparison of the SED of the raw data (without point sources) and the three different models in a very thin latitude stripe covering the Galactic plane. The grey triangles show the difference in the raw data west minus east. All models give similar results.

Fit the spectra with a power-law and a cutoff function. Fit the spectra with IC and pi0 models.

4.3. IC model

IC radiation is produced in scattering processes of relativistic electrons on photons of the ISRF. The spectrum of the IC gamma radiation depends on the density of ISRF photons, the density of electrons and the differential Klein-Nishina cross section $d\sigma_{IC}/dE_\gamma$, taken from (?):

$$\left(\frac{dn}{dE}\right)_{\gamma,IC} = \int \int \left(\frac{dn}{dE}\right)_{ISRF} \frac{d\sigma_{IC}}{dE_\gamma} \left(\frac{dn}{dE}\right)_e dE_{ISRF} dE_e. \quad (5)$$

The ISRF has three main components: starlight, IR and CMB. The first two components are taken from (???). For the CMB a thermal spectrum of 2.73 K is used. We assume that the distribution of electrons follows a powerlaw with a potential cutoff and determine the normalization n_e , spectral index γ_e and cutoff energy E_{cut} by fitting the IC spectrum(5) to the diffuse *Fermi* data using Poisson likelihood. Point sources are masked as described in Section 3. Figure 7 shows the residual spectrum in the low-energy model within the latitude stripes $b \in (-2^\circ, 2^\circ)$ and $b \in (-6^\circ, -2^\circ)$. The dotted line represents the best-fit IC spectrum.

4.4. Pion model

In collisions of CR protons and the interstellar gas neutral pions are created that decay into gamma-ray photons. The spectrum of the gamma radiation depends on the density of interstellar gas n_H , the density and velocity of CR protons and the cross section to produce gamma rays in a proton-nucleus collision:

$$\left(\frac{dn}{dE dt}\right)_\gamma = \int n_H \frac{d\sigma_p}{dE_\gamma} v_p \left(\frac{dn}{dT}\right)_p dT_p. \quad (6)$$

...

5. Conclusions

For the ROI, $b \in (-2^\circ, 2^\circ)$, $\ell \in (-10^\circ, 0^\circ)$, the total energy density in electrons with energy above $E_0 = 1$ GeV is given by the integral of the electron spectrum that was found in Section 4.3:

$$\frac{dE_{tot}}{dV} = \int_{E_0}^{\infty} \left(E \frac{dN}{dE}\right)_e dE = 3.8 \times 10^{-14} \text{ erg/cm}^3. \quad (7)$$

Assuming a distance of 8 kpc to the ROI, the volume of the ROI is $V = 0.54 \text{ kpc}^3 = 1.58 \times 10^{64} \text{ cm}^3$. The total energy content of the ROI in electrons above 1 GeV is $E_{tot} = 6 \times 10^{50} \text{ erg}$, which corresponds to the CR energy output of 60 SNe.

Using the result from Section 4.4 we find an energy density in protons of $dE_{tot}/dV = 6.6 \times 10^{-13} \text{ erg/cm}^3$ and a total energy content of $E_{tot} = 1 \times 10^{52} \text{ erg}$. However, the gas density in the inner Galaxy is probably higher than $n_H = 1/\text{cm}^3$ as assumed in Section 4.4, resulting in an energy content in protons of the same order of magnitude as the energy density in electrons.

To estimate the maximal propagation distance of electrons, we start with a diffusion equation taking into account diffusion and energy loss $b_{IC}(E)$ via IC. From the solution we read off the diffusion distance for electrons with energy $E_0 = 1 \text{ TeV}$:

$$\langle x \rangle^2 = 2 \int_{E_0}^E \frac{D(E)}{b_{IC}(E)} dE = 1300 \text{ pc}. \quad (8)$$

with a spatially constant diffusion coefficient $D(E) = D_0 \left(\frac{E}{1 \text{ GeV}}\right)^\delta$, where we take values of the local diffusion coefficient: $D_0 = 3 \times 10^{28} \text{ cm}^2/\text{s} = 100 \text{ pc}^2/\text{kyr}$ and $\delta = 0.4$. The energy loss $b_{IC}(E)$ is Since the diffusion distance of the electrons exceeds the spatial size of the ROI, the electrons cannot be confined. Therefore, we find that a transient process is favoured. The energy losses of protons exceed the energy losses of electrons by far, therefore the same applies for protons.

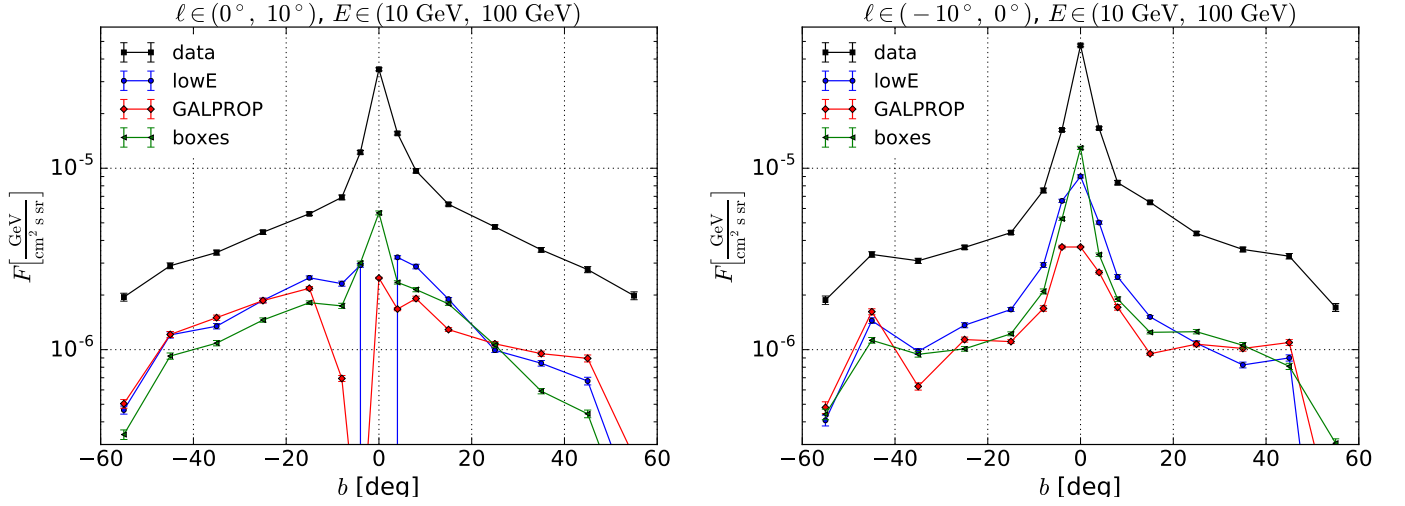


Fig. 5: Latitude profiles of the different models.

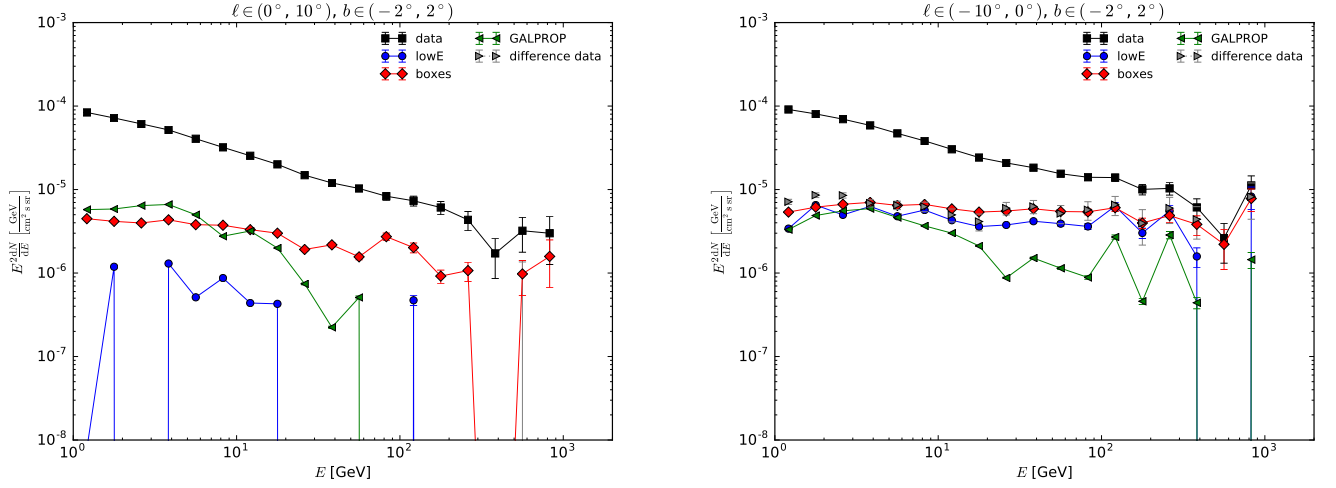


Fig. 6: Comparison of SED of all models.

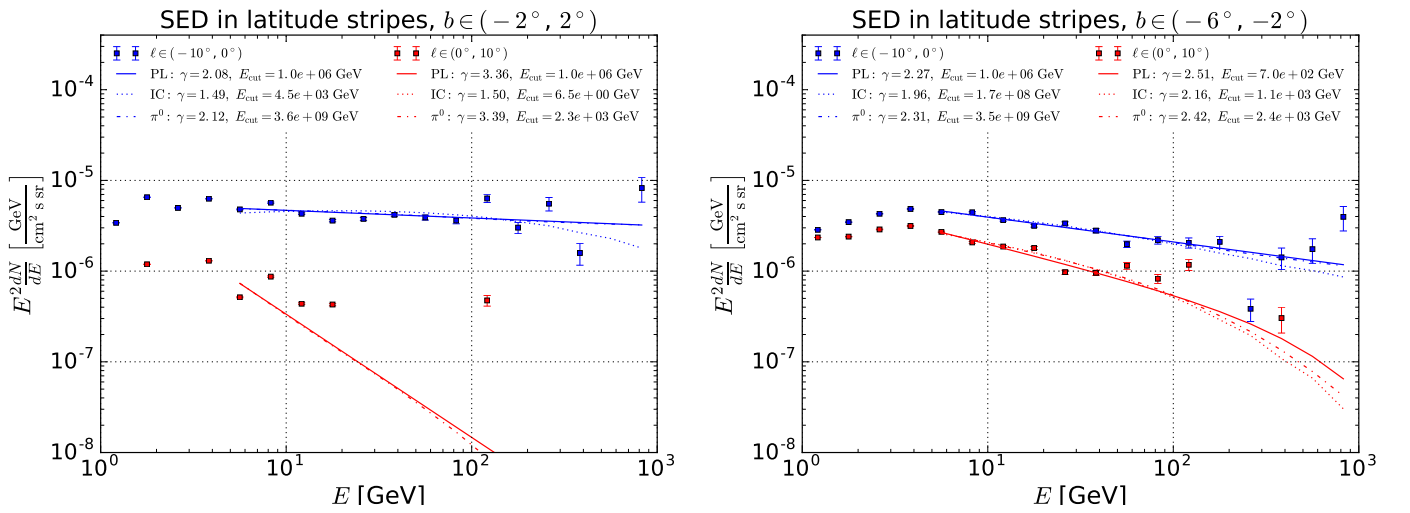


Fig. 7: SED of low-energy model with powerlaw and particle spectra fits.

With the local diffusion coefficient we find an escape time for both electrons and protons of

$$T = \frac{\Delta x^2}{2D(E)} = 70 \text{ kyr.} \quad (9)$$

References

- Acero, F., Ackermann, M., Ajello, M., et al. 2016, ApJS, 223, 26
Ackermann, M., Ajello, M., Albert, A., et al. 2017, ApJ, 840, 43
Górski, K. M., Hivon, E., Banday, A. J., et al. 2005, ApJ, 622, 759

Appendix A: Appendix

If we need one.